# Electromechanical Modeling and Normal Form Analysis of an Aeroelastic Micro-Power Generator

AMIN BIBO, GANG LI AND MOHAMMED F. DAQAQ*

*Department of Mechanical Engineering, Clemson University, Clemson, SC 29634, USA*

**ABSTRACT:** Combining theories in continuous-systems vibrations, piezoelectricity, and fluid dynamics, we develop and experimentally validate an analytical electromechanical model to predict the response behavior of a self-excited micro-power generator. Similar to music-playing harmonica that create tones via oscillations of reeds when subjected to air blow, the proposed device uses flow-induced self-excited oscillations of a piezoelectric beam embedded within a cavity to generate electric power. To obtain the desired model, we adopt the nonlinear Euler–Bernoulli beam's theory and linear constitutive relationships. We use Hamilton's principle in conjunction with electric circuits theory and the inextensibility condition to derive the partial differential equation that captures the transversal dynamics of the beam and the ordinary differential equation governing the dynamics of the harvesting circuit. Using the steady Bernoulli equation and the continuity equation, we further relate the exciting pressure at the surface of the beam to the beam's deflection, and the inflow rate of air. Subsequently, we employ a Galerkin's descritization to reduce the order of the model and show that a single-mode reduced-order model of the infinite-dimensional system is sufficient to predict the response behavior. Using the method of multiple scales, we develop an approximate analytical solution of the resulting reduced-order model near the stability boundary and study the normal form of the resulting bifurcation. We observe that a *Hopf* bifurcation of the *super-critical* nature is responsible for the onset of limit-cycle oscillations.

*Key Words:* energy harvesting, piezoelectric, aeroelasticity.

## INTRODUCTION

TODAY, many critical electronic devices, such as those used in wireless sensing and health monitoring, are becoming smaller, and more energy efficient requiring minute amounts of power to function. For instance, a wireless transponder for data transmission can operate efficiently with less than 1 mW of power (Gregori et al., 2004; Kim et al., 2007). A sensor interface chip for health monitoring has an average power consumption of 48 μW (Baerta et al., 2006; Bracke et al., 2007). These, and many other similar low-power consumption devices, are currently being powered using batteries that have not kept pace with their demands, especially in terms of energy density (Roundy et al., 2003; Paradiso and Starner, 2005). In addition, batteries have a finite life span requiring regular replacement or recharging, which, in many cases, is a very cumbersome and time-consuming process.

In light of the very low-power consumption of these electronics and different challenges associated with battery technology, scavenging, otherwise, wasted energy from the ambient environment can provide a solution to autonomously power and maintain these systems. To achieve this goal, scalable, low-maintainace, and easy to design micropower generators (MPGs) have been recently introduced as means to transform wasted ambient energy, e.g., thermal, solar, wind, and vibrations into electricity, (Roundy et al., 2003; Arms et al., 2005; duPlessis et al., 2005; Roundy and Wright, 2005; Inman and Grisso, 2006).

In the last couple of years, aerodynamic energy fields such as wind have attracted specific attention due to their abundance (Allen and Smits, 2001; Liao et al., 2003; Robbins et al., 2006; Simpson et al., 2008; Tang et al., 2009; Zhu et al., 2009; Barrero-Gil et al., 2010; Erturk et al., 2010). Unfortunately, traditional wind turbine designs that are based on an electromagnetic rotary-type generators suffer from scalability issues because their performance drops significantly with their size. Mitcheson et al. (2008) reported that the power coefficient of a rotary wind turbine can drop from 0.59 which corresponds to the Betz limit to less than 0.1 as the size of the turbine decreases. This is a result of relatively high viscous drag on the blades at low Reynolds numbers (Lissaman, 1983), bearing and thermal losses which increase significantly as size decreases, and high electromagnetic interferences. In addition to performance

*Author to whom correspondence should be addressed.
E-mail: mdaqaq@clemson.edu
Figures 1–4 and 6–14 appear in color online: http://jim.sagepub.com



1045-389X/11/06 0577–16 $10.00/0 DOI: 10.1177/1045389X11400929

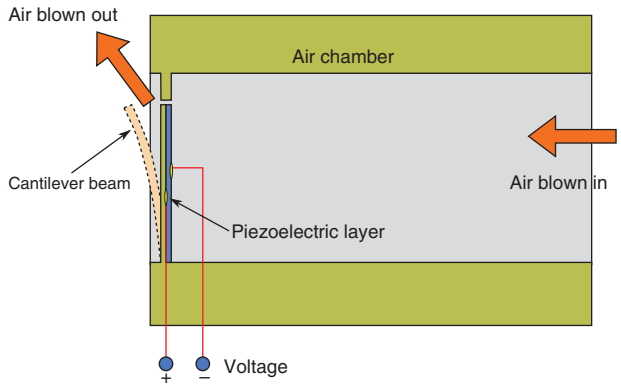


***Figure 1.*** *Operation concept of the self-excited MPG.*

issues, the design and fabrication of traditional small-scale rotary-type generators that require a rotor, a stator, magnets, wirings, and blades is a very complex and expensive process. This makes their actual implementation for compact applications an astounding task.

Motivated by the obvious need for a compact, scalable, cheap, and low-maintenance wind energy generator, we have recently introduced a new concept for an energy harvester which uses wind energy to maintain remote low-power consumption sensors (St. Clair et al., 2009, 2010). Inspired by music-playing harmonica, the harvester shown in Figure 1 consists of a piezoelectric cantilever uni-morph structure embedded within a cavity to mimic the vibrations of the reeds in a harmonica when subjected to air blow. The operation principle of the harvester is simple. Wind blows into the chamber and tries to escape through the small aperture between the cantilever (reed) and the supporting structure. The sudden change in area causes the flow to separate from the cantilever at the sharp edge which causes the velocity to increase rapidly. This, in turn, produces a pressure drop across the cantilever. The resulting pressure drop bends the cantilever which causes the aperture area to increase. Consequently, the flow velocity drops and the pressure drop decreases. The mechanical restoring force pulls the beam back decreasing the aperture area and the process is repeated. These periodic fluctuations in the pressure cause the beam to undergo *self-sustained* oscillations. The resulting periodic strain in the piezoelectric layer produces an electric field which can be channeled as a current to an electric device.

In previous efforts (St. Clair et al., 2009, 2010), the authors introduced the basic physics of this concept and proved its feasibility. In this study, we focus on obtaining and validating a non-linear aero-electro-mechanical model to represent the system dynamics. The availability of this model is essential toward optimizing the design parameters for enhanced power density and to minimize the cut-on wind speed of the device. To achieve this goal, the rest of the manuscript is organized as follows: We first discuss the basic physics of the generator in the second Section. We follow that by a development of an electromechanical model to predict its behavior in the third Section. Using a Galerkin descritization, we reduce the order of the model in the fourth Section and study its convergence in the fifth Section. In the sixth Section, we experimentally validate the reduced-order model. Using the resulting model, we construct the normal form of the bifurcation near the stability boundary in the seventh Section. Finally, in eighth Section, we present our conclusions and recommendations for future work.

## OPERATION CONCEPT

The operation concept of this device is based on a non-linear phenomenon known as *self-excited* or *self-sustained* oscillations. This phenomenon can be best explained by studying the dynamics of the long-celebrated Van der Pol oscillator whose equation of motion can be written as (Strogatz, 2000):

$$\ddot{x}+\mu(x^2-1)\dot{x}+x=0, \quad \mu \geq 0. \tag{1}$$

Equation (1) is a simple harmonic oscillator but with a linear negative damping term $-\mu\dot{x}$ and a non-linear positive damping term $\mu x^2\dot{x}$. Note that negative damping pumps energy into the system while positive damping pumps energy out of the system. As such, for small oscillations, $|x|<1$, the non-linear positive damping is very small and the effective damping of the system is negative causing small amplitude oscillations to grow. However, as $|x|>1$, the non-linear damping becomes large and the effective damping becomes positive causing large amplitudes to decay. At one point, the energy dissipated over one cycle balances the energy pumped and the system settles into self-sustained fixed-amplitude oscillations that are called *limit cycles*.

In the case of this MPG concept, self-excited oscillations occur when the volumetric flow rate past the cantilever is large enough such that the energy pumped into the structure via non-linear pressure forces offsets the intrinsic linear damping in the system which consists of the structural damping and electric damping due to electric energy generation. One can think of this process as a non-linear feedback mechanism in which the motion of the cantilever produces a disturbance in the potential flow that feeds enough energy back to the structure to overcome the internal damping (Hilaire, 1976; Fletcher, 1992; Tarnopolsky et al., 2001).

The onset of the limit-cycle oscillations necessary for energy harvesting (cut-on wind speed) is governed by a threshold combination of the flow and design parameters known as the *Hopf bifurcation* point. Below that point, the energy pumping mechanism cannot overcome the damping mechanism and the structure settles at a static equilibrium and hence no power can be harvested

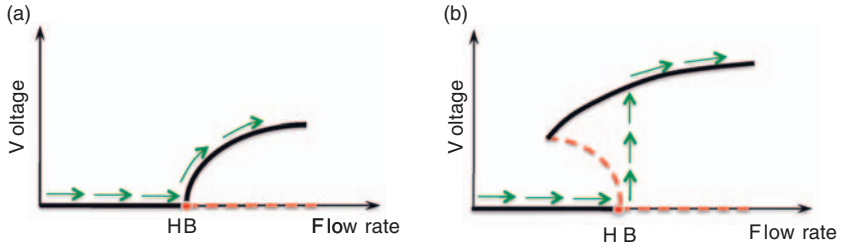


***Figure 2.*** *Two scenarios for the voltage response of the MPG as the flow rate increases: (a) supercritical Hopf bifurcation and (b) subcritical Hopf bifurcation.*

as shown in Figure 2(a). Beyond that threshold, the non-linear pressure forces overcome the intrinsic damping in the system and the beam undergoes limit-cycle oscillations.

Not only does the combination of the design parameters determine the cut-on wind speed but they also determine the nature of the response beyond it (*bifurcation nature*). As shown in Figure 2(a), when the bifurcation is *supercritical* and the flow rate exceeds the threshold value, small-amplitude limit-cycle oscillations about the former static position are born. On the other hand, when the bifurcation is *subcritical* as shown in Figure 2(b), the output voltage jumps to a distant attractor which can be another fixed point, a large-amplitude limit cycle, or a chaotic attractor.

From a mathematical perspective, this bifurcation threshold represents a point at which two or more complex-conjugate eigenvalues associated with the Jacobian of the system dynamics transversally cross the imaginary axis from the left- to the right-half of the complex plane. With this understanding, it becomes evident that the ability of this device to generate energy depends on the onset of the bifurcation which has a *complex* and, as of today, *unknown* dependence on the design parameters and flow characteristics.

## THE ELECTROMECHANICAL MODEL

To resolve the unknown dependence of the dynamics on the the design parameters, we obtain a non-linear electromechanical model that governs the response of the system shown in Figure 3. As air of flow rate, $U_0$, blows into one side of a large reservoir, its speed drops causing a pressure $P_A(t)$ to build on the top side of the cantilever which forces the cantilever to deflect by $w(s,t)$ and elongate by $u(s,t)$. Air escapes with a flow rate $U(t)$ through the aperture between the cantilever and the support. Variations in the pressure produce a time-varying strain in the piezoelectric layer, which produces a voltage $V(t)$ across an electric load, $R$.

As depicted graphically in Figure 4, five equations are necessary to describe the evolution of the system dynamics which is governed by five parameters, namely, the exciting pressure, $P_A(t)$, the beam's deflection and elongation, $w(s,t)$ and $u(s,t)$, the flow rate through the aperture, $U(t)$, and the voltage developed across the load, $V(t)$; with the last being the critical parameter necessary to calculate the output power of the harvester.

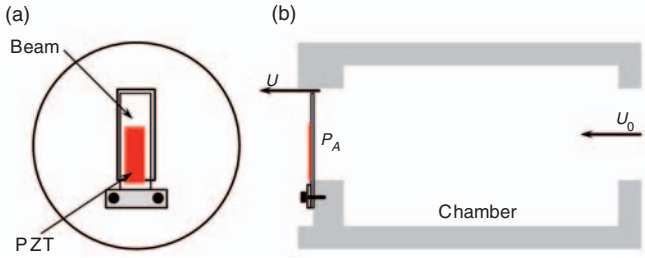


***Figure 3.*** *Schematic of the self-excited MPG: (a) front view and (b) sectional view.*

### Non-linear Strain–Displacement Relationship

We start by developing the strain–displacement relationships of the beam. For a slender beam similar to the one considered here, shear deformations and rotary inertia can be neglected allowing for the adoption of the non-linear Euler–Bernoulli's beam theory to model the beam's response. According to Euler's theory, the flexural dynamics of the beam can be described using a longitudinal displacement, $u(s,t)$, and a transversal displacement, $w(s,t)$, Figure 4(b), where $s$ denotes the arclength and $t$ denotes time. To describe a beam element before and after deformation, two cartesian coordinate systems are utilized: the $(x,y,z)$ is considered to be global, while the $(\bar{x},\bar{y},\bar{z})$ is a local system, and they are related through a transformation matrix corresponding to the rotation around the $\bar{y}$-axis. Using Figure 4(b), it follows that the longitudinal elongation of the beam element can be written as (Nayfeh, 2004):

$$e = \sqrt{(\mathrm{d}s + \mathrm{d}u)^2 + \mathrm{d}w^2} - \mathrm{d}s. \tag{2}$$

Dividing Equation (2) by the element length, d$s$, the strain along the neutral axis of the differential element becomes:

$$\epsilon_0 = \sqrt{(1+u')^2 + w'^2} - 1, \tag{3}$$

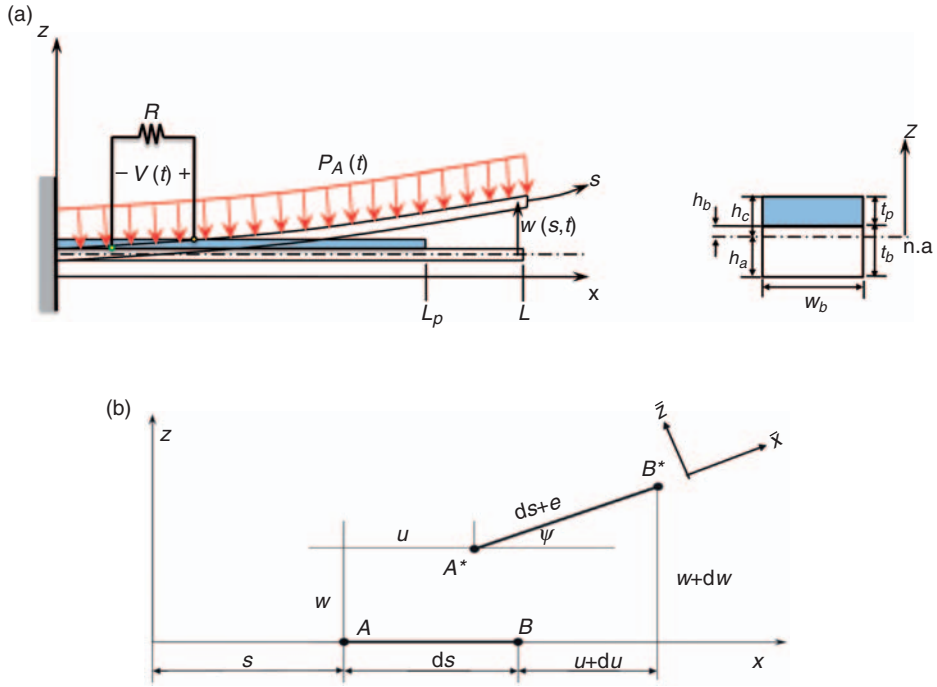


***Figure 4.*** *(a) Schematic of the beam harvester and (b) Deformation of a differential beam element.*

where the over-prime denotes a derivative with respect to the arclength, $s$. Using a quadratic Taylor expansion of Equation (3), we obtain:

$$\epsilon_0 = u' + \frac{w'^2}{2}. \tag{4}$$

Due to rotation of the differential beam element, the strain at a point having the coordinates $(\bar{x}, \bar{y}, \bar{z})$ relative to the neutral axis can be written in terms of the beam's curvature using:

$$\epsilon = -\bar{z}\frac{\mathrm{d}\psi}{\mathrm{d}s}. \tag{5}$$

Referring to Figure 4(b), the rotation angle, $\psi(s, t)$, can be expressed as:

$$\psi(s,t) = \tan^{-1}\left[\frac{w'(s,t)}{1+u'(s,t)}\right]. \tag{6}$$

Substituting Equation (6) back into Equation (5), then expanding the outcome in a Taylor expansion up to cubic terms, yields:

$$\epsilon = -\bar{z}\left[w'' - w''u' - w'u'' - w''w'^2\right]. \tag{7}$$

Adding Equations (4) and (7), the total axial strain can be written as:

$$\epsilon_x = u' + \frac{w'^2}{2} - \bar{z}\left[w'' - w''u' - w'u'' - w''w'^2\right]. \tag{8}$$

## Stress–Strain Relationships

The stress–strain relationships of the beam and the piezoelectric layer are assumed to follow the linear constitutive equations given by:

$$\sigma_x^b = Y^b\epsilon_x^b, \tag{9}$$

$$\sigma_x^p = Y^p\left[\epsilon_x^p - d_{31}E_3\right], \tag{10}$$

where $\sigma_x$ and $\epsilon_x$ are the stress and the strain in the axial direction, respectively; $Y$ is Young's modulus, $d_{31}$ the piezoelectric constant, and $E_3$ the electric field developed in the piezoelectric layer. Here, the superscript $p$ and $b$ stand for the piezoelectric and structural layers, respectively.

Assuming that the charge has a homogeneous distribution along the piezoelectric layer, the electric field can be related to the voltage, $V(t)$, developed across the electric load, $R$, and the piezoelectric layer thickness, $t_p$, using $E_3 = -V(t)/t_p$. Utilizing Ohm's law, the voltage can be further related to the current via $V(t) = R\dot{Q}_R(t)$, where $\dot{Q}_R$ is the current passing through the load, see Figure 5. Here, the over-dot indicates a derivative with respect to time. Substituting the aforementioned relations back into Equation (10), yields:

$$\sigma_x^p = Y^p\left[\epsilon_x^p + \frac{d_{31}}{t_p}R\dot{Q}_R(t)\right]. \tag{11}$$

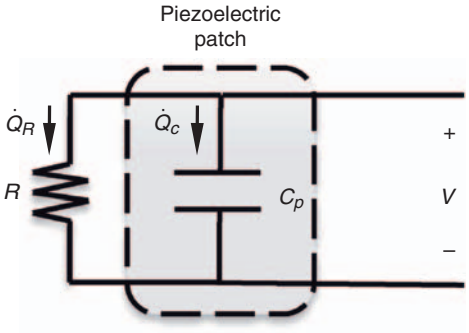


***Figure 5.*** *Schematic of the harvesting circuit.*

## Equations of Motion and Boundary Conditions

To obtain the equations of motion, we use Hamilton's variational principle which states that:

$$\int_{t_1}^{t_2} \delta\mathcal{L} + \delta\mathcal{W}^{ext}\mathrm{d}t = 0, \tag{12}$$

where $t_1$ to $t_2$ is any arbitrary time interval, δ the virtual operator, $\mathcal{L} = T - U$ the Lagrangian, and $\mathcal{W}^{ext}$ a non-conservative work term. The kinetic energy, $T$, of the system can be expressed as:

$$T = \frac{1}{2}\int_0^L M(s)\left(\dot{u}^2 + \dot{w}^2\right)\mathrm{d}s, \tag{13}$$

where $M(s)$ is the mass per unit length of the beam given by:

$$M(s) = W_b\rho^b t_b + W_p\rho^p t_p\left[H(s) - H(s - L_p)\right]. \tag{14}$$

Here, $\rho$ is the mass density, $t$ and $W$ are the associated thickness and width of the layer, and $H(s)$ is the Heaviside function.

The total potential energy of the system, $U$, consists of the strain energy of the composite beam in addition to the electric potential stored in the capacitive piezoelectric layer. These can be expressed as:

$$U = \frac{1}{2}\int_{\mathcal{V}}\left(\sigma_x^b\epsilon_x^b + \sigma_x^p\epsilon_x^p\right)\mathrm{d}\mathcal{V} - \frac{1}{2}\int_{\mathcal{V}} E_3 D_3\mathrm{d}\mathcal{V}, \tag{15}$$

where $\mathcal{V}$ is the domain and $D_3$ the electric displacement given by the following linear piezoelectric constitutive relation:

$$D_3 = d_{31}Y^p\epsilon_x^p - e_{33}E_3, \tag{16}$$

where $e_{33}$ is the permittivity at constant strain.

Replacing the electric field, $E_3$, in Equation (16) again by $-R\dot{Q}_R/t_p$, then substituting Equations (8), (9), (11), and (16) back into Equation (15), and carrying the integration over the thickness of each layer, we obtain:

$$\begin{aligned} U = \frac{1}{2}\int_0^L \Bigg[ & YA(s)\left(u'^2 + u'w'^2 + \frac{1}{4}w'^4\right) \\ & + YI(s)\left(w''^2 - 2w''^2w'^2 - 2w''^2u' - 2w'w''u''\right) \\ & + 2\theta(s)\left(w'' - w''u' - w'u'' - w''w'^2\right)R\dot{Q}_R(t)\Bigg]ds \\ & - \frac{1}{2}C_p(R\dot{Q}_R(t))^2, \end{aligned} \tag{17}$$

where $YA(s)$, $YI(s)$, $\theta(s)$, and $C_p$ are, respectively, the axial stiffness, the bending stiffness, the electromechanical coupling, and the piezoelectric capacitance:

$$\begin{aligned} YA(s) &= W_p t_p Y^p\left[H(s) - H(s - L_p)\right] + W_b t_b Y^b, \\ YI(s) &= \frac{1}{3}\left(W_b Y^b\left(h_b^3 - h_a^3\right) + W_p Y^p\left(h_c^3 - h_b^3\right)\right) \\ &\quad \times \left[H(s) - H\left(s - L_p\right)\right] \\ &\quad + \frac{W_b Y^b t_b^3}{12}\left[H\left(s - L_p\right) - H(s - L)\right], \\ \theta(s) &= \frac{-W_p Y^p d_{31}}{2t_p}\left(h_c^2 - h_b^2\right)\left[H(s) - H(s - L_p)\right], \\ C_p &= \frac{e_{33}W_p L_p}{t_p}. \end{aligned}$$

Here, $h_a$, $h_b$, and $h_c$ are the thickness boundaries measured from the neutral axis of the beam as showed in Figure 4(a). The location of the neutral axis is determined relative to the bottom surface of the composite beam by recalling that stresses through the cross-section must be in equilibrium, which yields:

$$h_a = -\frac{1}{2}\frac{Y^b W_b t_b^2 + 2Y^p W_p t_p t_b + Y^p W_p t_p^2}{Y^b W_b t_b + Y^p W_p t_p}. \tag{18}$$

### *INEXTENSIBILITY CONDITION*

Assuming that the beam is inextensible, i.e., the elongation along the neutral axis is equal zero, we can relate the longitudinal displacement, $u(s, t)$, to the transversal displacement, $w(s, t)$. This condition is valid only when the beam has a zero geometric boundary condition at one end; similar to the cantilever beam considered here. With that, Equation (3) yields:

$$(1 + u')^2 + w'^2 = 1. \tag{19}$$

Integrating Equation (19) twice with respect to the arclength $s$, taking into account the boundary conditions at the clamped end, we obtain:

$$u = -\frac{1}{2}\int_0^s w'^2\mathrm{d}s. \tag{20}$$

Using Equations (13), (17), and (19), the Lagrangian of the system can be written as:

$$\mathcal{L} = \frac{1}{2}\int_0^L \Big\{ M(s)\big(\dot{u}^2 + \dot{w}^2\big) - YA(s)\big(u'^2 + u'w'^2 + \frac{1}{4}w'^4\big) - YI(s)\big(w''^2 - 2w''^2w'^2 - 2w''^2u' - 2w'w''u''\big) - 2\theta(s)\big(w'' - w''u' - w'u'' - w''w'^2\big)R\dot{Q}_R(t) + \lambda(s,t)\Big[1 - (1+u')^2 - w'^2\Big]\Big\}\mathrm{d}s + \frac{1}{2}C_p(R\dot{Q}_R(t))^2, \quad (21)$$

where $\lambda(s,t)$ is a Lagrange multiplier introduced to account for the inextensibility constraint.

*NON-CONSERVATIVE FORCES*

The influence of the non-conservative forces can be captured by introducing the general virtual-work term:

$$\delta\mathcal{W}^{ext} = \int_0^L \big(F_u^*\delta u + F_w^*\delta w + F_\lambda^*\delta\lambda\big)\mathrm{d}s + F_{Q_R}^*\delta Q_R, \quad (22)$$

where

$$F_u^* = 0,\ \ F_w^* = [WP_A(t) - c_a\dot{w}],\ \ F_\lambda^* = 0,\ \ F_{Q_R}^* = -R\dot{Q}_R(t).$$

The term associated with $F_w^*$ represents the work done by the pressure forces on the beam surface and mechanical viscous damping. Here, the gauge pressure, $P_A(t)$, is assumed to be uniform over the beam area and $c_a$ denotes a viscous damping coefficient. The term associated with $F_{Q_R}^*$ is used to account for electric damping.

Substituting Equations (21) and (22) back into Equation (12) yields the equations of motion and boundary conditions in the following general form (Meirovitch, 1997):

$$\frac{\partial\ell}{\partial r_i} - \frac{\partial}{\partial s}\left(\frac{\partial\ell}{\partial r_i'}\right) + \frac{\partial^2}{\partial s^2}\left(\frac{\partial\ell}{\partial r_i''}\right) - \frac{\partial}{\partial t}\left(\frac{\partial\ell}{\partial\dot{r}_i}\right) = -F_i^*, \quad (23)$$

$$B1_i = \left\{\left[\frac{\partial\ell}{\partial r_i'} - \frac{\partial}{\partial s}\left(\frac{\partial\ell}{\partial r_i''}\right)\right]\delta r_i\right\}_{s=0}^{s=L} = 0,$$

$$B2_i = \left\{\left[\frac{\partial\ell}{\partial r_i''}\right]\delta r_i'\right\}_{s=0}^{s=L} = 0, \quad (24)$$

where $\mathcal{L} = \int_0^L \ell\,(s,t)\mathrm{d}s$ and $r_i \equiv (u(s,t),\ w(s,t),\ Q_R(t))$.

*LONGITUDINAL DYNAMICS*

When $r_i \equiv u(s,t)$, Equations (23) and (24) yield:

$$\big[YI(s)w''^2\big]' + \frac{1}{2}R\dot{Q}_R[2\theta(s)w'']' - \left[\lambda(1 - \frac{1}{2}w'^2)\right]' - \big[YI(s)w'w'' + \theta(s)R\dot{Q}_Rw'\big]'' - M(s)\left[\frac{1}{2}\int_0^s(\ddot{w}')^2\mathrm{d}s\right] = 0, \quad (25)$$

and the boundary conditions:

$$u = 0 \quad \text{at} \quad s = 0,$$

$$YI(s)w''^2 + \theta(s)w''R\dot{Q}_R - \lambda(1 - \frac{1}{2}w'^2) - \big[YI(s)w'w'' + \theta(s)R\dot{Q}_Rw'\big]' = 0 \quad \text{at} \quad s = L, \quad (26)$$

Using Equations (25) and (26), we can solve for $\lambda(s,t)$ and obtain to second order:

$$\lambda(s,t) = YI(s)w''^2 - \big[YI(s)w'w'' + \theta(s)R\dot{Q}_Rw'\big]' + \theta(s)w''R\dot{Q}_R - \int_L^s M(s)\left[\frac{1}{2}\int_0^s(\ddot{w}')^2\mathrm{d}s\right]\mathrm{d}s. \quad (27)$$

*TRANSVERSAL DYNAMICS*

When $r_i \equiv w(s,t)$, Equations (20), (23), (24), and (27) yield the following equation of motion governing the transversal vibrations of the beam:

$$M(s)\ddot{w} + [YI(s)w'']'' + \big[w'(YI(s)w'w'')'\big]' + c_a\dot{w} + \left[w'\int_L^s M(s)\left[\frac{1}{2}\int_0^s(\ddot{w}')^2\mathrm{d}s\right]\mathrm{d}s\right]' + 3[\theta(s)w'w''V(t)]' + \left[\theta'(s)V(t)(1 + \frac{1}{2}w'^2)\right]' = W_bP_A(t), \quad (28)$$

and the associated boundary conditions:

$$w = w' = 0, \quad \text{at} \quad s = 0; \quad w'' = w''' = 0 \quad \text{at} \quad s = L. \quad (29)$$

Equation (28) contains terms similar to those obtained by many researches for vibratory energy harvesters (duToit and Wardle, 2007; Erturk and Inman, 2008; Osorio and Daqaq, 2009). However, the difference is that these equations include non-linear stiffness and inertia terms, the fourth and fifth terms in Equation (28), respectively; as well as, the non-linear electromechanical coupling terms, the sixth and second part of the seventh term, respectively. The excitation term, which is normally in the form of a base excitation in vibratory energy harvesters, is replaced by the unknown dynamics of the surface pressure, $P_A(t)$.

*ELECTRIC CIRCUIT DYNAMICS*

Setting $r_i \equiv Q_R(t)$ in Equations (23) and (24), we obtain the following equation for the electric circuit dynamics:

$$\frac{\partial}{\partial t}\left[\int_0^L \theta(s)(w'' + \frac{1}{2}w''w'^2)\mathrm{d}s\right] - C_p\dot{V}(t) = \dot{Q}_R. \quad (30)$$

Since the piezoelectric element and the resistive load are connected in parallel, Figure 5, we can replace the

current passing through the resistor, $\dot{Q}_R$, by $V(t)/R$. With that, Equation (30) becomes:

$$C_p\dot{V}(t)+\frac{1}{R}V(t)=\frac{\partial}{\partial t}\left[\int_0^L \theta(s)(w''+\frac{1}{2}w''w'^2)\mathrm{d}s\right]. \quad (31)$$

*PRESSURE DYNAMICS*

The only remaining unknown in the model is the pressure distribution on the cantilever surface. This distribution which we denoted as $P_A(t)$ depends on the inflow rate of air, $U_0$, the beam deflection, $w(s,t)$, and the flow rate through the aperture, $U(t)$. To obtain an equation that governs the dynamics of the pressure exerted on the cantilever, we invoke several assumptions on the flow field near the cantilever. First, we assume that the flow near the beam and through the aperture is invisid knowing the very low viscosity of air at normal temperatures. Also, following studies by Ricot et al. (2005) on the dynamics of harmonica, we assume that the flow stream through the aperture is irrotational, two dimensional, and laminar. Tarnopolsky et al. (2000) has also shown experimentally that unsteadiness of the flow through the aperture has a little influence on the dynamics of harmonica reeds and hence can be neglected. With these assumptions, we can utilize the steady Bernoulli equation to relate the air pressure on the surface, $P_A(t)$, to the volumetric air flow rate through the aperture, $U(t)$, as following (Fletcher, 1992):

$$P_A(t)=\frac{1}{2}\rho_a\frac{U^2(t)}{C_c^2A^2(t)}, \quad (32)$$

where $\rho_a$ is the density of air, $C_c$ is the flow contraction coefficient for flow through a sharp edged slit (Munson et al., 2009), and $A(t)$ is the total exit area of the aperture given by:

$$A(t)=2\int_0^L\left[w^2(s,t)+b^2\right]^{\frac{1}{2}}\mathrm{d}s+W_b\left[w^2(L,t)+b^2\right]^{\frac{1}{2}}. \quad (33)$$

Here, $b$ is the width of the clearance gap around the beam. Using the continuity equation, we further relate the pressure to the steady inflow $U_0$, the outflow $U(t)$, and the change in reservoir volume caused by beam vibrations using:

$$\dot{P}_A(t)=\frac{\rho_a c^2}{V_r}\left[U_0-U(t)-W_b\frac{\partial}{\partial t}\int_0^L w(s,t)\mathrm{d}s\right], \quad (34)$$

where $c$ is the speed of sound, and $V_r$ is the volume of the chamber. Solving Equation (32) for $U(t)$, then substituting into Equation (34), we obtain:

$$\dot{P}_A(t)=\frac{\rho_a c^2}{V_r}\left[U_0-C_cA(t)\left(\frac{2}{\rho_a}P_A(t)\right)^{\frac{1}{2}}-W_b\frac{\partial}{\partial t}\int_0^L w(s,t)\mathrm{d}s\right]. \quad (35)$$

For known $U_0$ and system design parameters, the response characteristics of the harvester can now be determined by solving Equations (28), (31), and (35).

## REDUCED-ORDER MODELING

We utilize a Galerkin expansion to discretize the partial differential equation governing the motion of the system. We express the spatio-temporal function representing the transversal vibrations of the beam, $w(s,t)$, in the form of a convergent series of eigenfunctions multiplied by unknown temporal coordinates, i.e., we let:

$$w(s,t)=\sum_{i=1}^{\infty}\phi_i(s)q_i(t), \quad (36)$$

where $q_i(t)$ is the unknown temporal coordinates and $\phi_i(s)$ are chosen as the orthonormal mass-normalized mode shapes of a cantilever beam. These can be written as:

$$\phi_i(s)=C_i\left[\cosh\frac{\lambda_i}{L}s-\cos\frac{\lambda_i}{L}s-\sigma_i\left(\sinh\frac{\lambda_i}{L}s-\sin\frac{\lambda_i}{L}s\right)\right], \quad (37)$$

where $\sigma_i$ is expressed as:

$$\sigma_i=\frac{\sinh\lambda_i-\sin\lambda_i}{\cosh\lambda_i+\cos\lambda_i}, \quad (38)$$

and the $\lambda_i$ and $C_i$ are obtained via:

$$1+\cosh\lambda_i\cos\lambda_i=0, \quad (39)$$

$$\int_0^L M(s)\phi_i^2(s)\mathrm{d}s=1. \quad (40)$$

Substituting Equation (36) into Equation (28), multiplying by $\phi_n(s)$, integrating over the length of the beam, and using the orthonormality properties of the chosen mode shapes yields the following set of non-linear ordinary differential equations:

$$\ddot{q}_n+2\zeta\omega_n\dot{q}_n+\omega_n^2q_n+\sum_{i,j,k}^{\infty}\mathcal{A}_{nijk}q_iq_jq_k+\sum_{i,j,k}^{\infty}\mathcal{B}_{nijk}q_i(\ddot{q}_jq_k+2\dot{q}_j\dot{q}_k+q_j\ddot{q}_k)+\left[\mathcal{D}_n+\sum_{i,j}^{\infty}\mathcal{C}_{nij}q_iq_j\right]\times V(t)=\mathcal{E}_nP_A(t), \qquad n=1,2,3,\ldots, \quad (41)$$

where

$$\omega_n^2 = \int_0^L \phi_n \left[ YI(s)\phi_i'' \right]'' \mathrm{d}s,$$

$$\mathcal{A}_{nijk} = \int_0^L \phi_n \left[ \phi_i' (YI(s)\phi_j'\phi_k'')' \right]' \mathrm{d}s,$$

$$\mathcal{B}_{nijk} = \frac{1}{2}\int_0^L \phi_n \left[ \phi_i' \int_L^s M(s) \left( \int_0^s \phi_j'\phi_k' \mathrm{d}s \right) \mathrm{d}s \right]' \mathrm{d}s,$$

$$\mathcal{C}_{nij} = 3\int_0^L \phi_n \left[ \theta(s)\phi_i'\phi_j'' \right]' \mathrm{d}s + \frac{1}{2}\int_0^L \phi_n \left[ \theta'(s)\phi_i'\phi_j' \right]' \mathrm{d}s,$$

$$\mathcal{D}_n = \int_0^L \phi_n \theta''(s) \mathrm{d}s,$$

$$\mathcal{E}_n = W_b \int_0^L \phi_n \mathrm{d}s.$$

Also, substituting Equation (36) into Equations (31) and (35), we obtain:

$$C_p \dot{V}(t) + \frac{1}{R} V(t) = \sum_n^\infty \mathcal{F}_n \dot{q}_n + \sum_{nij}^\infty \mathcal{G}_{nij} (\dot{q}_n q_i q_j + q_n \dot{q}_i q_j + q_n q_i \dot{q}_j), \quad (42)$$

and

$$\dot{P}_A(t) = \frac{\rho_a c^2}{V_r} \left[ U_0 - C_c A(t) \left( \frac{2}{\rho_a} P_A(t) \right)^{\frac{1}{2}} - \sum_n^\infty \mathcal{E}_n \dot{q}_n \right], \quad (43)$$

where

$$\mathcal{F}_n = \int_0^L \theta(s)\phi_n'' \mathrm{d}s,$$

$$\mathcal{G}_{nij} = \frac{1}{2}\int_0^L \theta(s)\phi_n''\phi_i'\phi_j' \mathrm{d}s,$$

$$A(t) = 2\int_0^L \left[ \sum_{ni}^\infty \phi_n \phi_i q_n q_i + b^2 \right]^{\frac{1}{2}} \mathrm{d}s + W_b \left[ \sum_{ni}^\infty \phi_n(L)\phi_i(L) q_n q_i + b^2 \right]^{\frac{1}{2}}. \quad (44)$$

## CONVERGENCE ANALYSIS

When the air flows into the chamber with flow rate $U_0$, the beam deflects into a new static position determined by the flow rate. If the flow rate is less than a certain threshold which we will denote as the *bifurcation* or cut-on flow rate, the pressure forces cannot overcome the intrinsic damping in the system and the beam settles at that static position. On the other hand, when the flow rate exceeds the cut-on threshold, the static solution loses stability via a *Hopf* bifurcation giving way to *limit-cycle* oscillations around it. Before we delve into the experimental validations of the derived model and its ability to predict this behavior, we seek to determine the minimum number of modes necessary for convergence. In other words, we want to determine the minimum number of modes to be kept in the Galerkin expansion such that the addition of any more modes does not affect the predictions of:

(i) the static response,
(ii) the cut-on flow rate (linear dynamic response), and
(iii) the amplitude of the limit cycles around it (non-linear dynamic response).

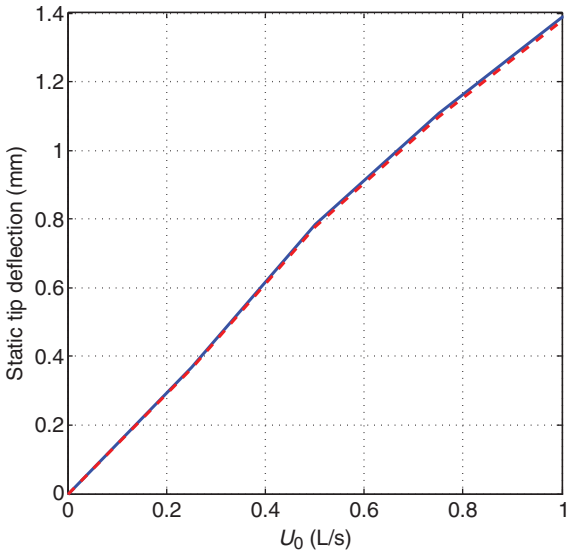


***Figure 6.*** *Static tip deflection of the beam using a single-mode approximation (solid) and three-mode reduced-order model (dashed).*

Toward that end, we express Equations (41), (42), and (43) in the state-space form as following:

$$\mathbf{x} = f(\mathbf{x}, U_0), \quad (45)$$

where $\mathbf{x} = \left[ q_1, \dot{q}_1, q_2, \dot{q}_2, \ldots, q_i, \dot{q}_i, \dot{P}_A, \dot{V} \right]$, $U_0$ is the input flow rate (*bifurcation parameter*), and $f(\mathbf{x}, U_0)$ is the non-linear vector field. To study the convergence of the static solution, the equilibrium points of the system are obtained by setting the right-hand side of Equation (45) to zero and solving the resulting non-linear algebraic equations, $f(\mathbf{x_0}, U_0) = 0$, for $\mathbf{x_0}$.

Figure 6 shows variation of the static tip deflection of the beam with the input flow rate using a single-mode and three-mode approximations. Results are obtained for the numerical parameters listed in Table 1. It can be seen clearly that the algebraic system yields only one physical solution and that the two curves are in excellent agreement. This implies that the static position is well-estimated using a single-mode assumption.

***Table 1. Geometric and material properties of the beam and piezoelectric layer.***

| Properties | |
|---|---|
| Modulus of elasticity, $Y^b$ (GPa) | 70 |
| Density, $\rho^b$ (kg/m$^3$) | 2700 |
| Length, $L_b$ (mm) | 60 |
| Width, $W_b$ (mm) | 16 |
| Thickness, $t_b$ (mm) | 0.25 |
| Gap width, $b$ (mm) | 0.2 |
| **Piezoelectric layer** | |
| Density, $\rho^p$ (kg/m$^3$) | 7850 |
| Length, $L_p$ (mm) | 13 |
| Width, $W_b$ (mm) | 16 |
| Modulus of elasticity, $Y^p$ (GPa) | 66 |
| Thickness, $t_p$ (mm) | 0.127 |
| Electromechanical coupling, $d_{31}$ (pm/V) | −190 |
| Permittivity, $e_{33}$ (nF/m) | 15.93 |
| **Other** | |
| Air density, $\rho_a$ (kg/m$^3$) | 1.2 |
| Speed of sound, $c$ (m/s) | 340 |
| Contraction coefficient, $C_c$ | 0.63 |
| Chamber volume, $V_r$ (L) | 2.4 |
| Electrical load, $R$ (KΩ) | 50 |

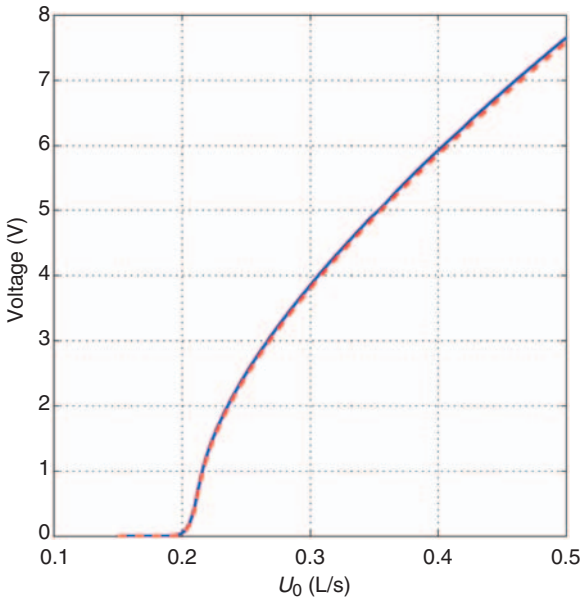


***Figure 7.*** *Voltage response of the beam using a single-mode approximation (solid) and a three-mode reduced-order model (dashed).*

To determine the minimum number of modes necessary to capture the linear dynamic response of the system, we obtain the eigenvalues of the response by finding the determinant of the Jacobian matrix evaluated at the fixed points. This yields a characteristic equation having $2n+2$ roots. Two of the resulting eigenvalues are always real and are associated with the harvesting circuit and pressure dynamics, respectively. The remaining $2n$ eigenvalues represent $n$ pairs of complex conjugate roots that describe the mechanical vibrations of the beam. The convergence of the reduced-order model is investigated by keeping a single mode in the series ($n=1$) and calculating the first four eigenvalues. The number of modes is then gradually increased and variation of these eigenvalues is monitored. Using a flow rate of $U_0=0.25$ L/s, we calculate the following eigenvalues by keeping one mode: $71.60 \pm 588.02i$, $-366.00$, and $-997.00$. Adding an additional mode, we obtain the following eigenvalues $72.99 \pm 587.80i$, $-360.69$, and $-977.37$. This yields a maximum error of less than 3% in all of the resulting eigenvalues. By adding a third mode, the maximum error drops to less than 0.5%. Furthermore, the bifurcation point representing the cut-on flow rate of the device was determined to be $U_{cr}=0.2$ L/s using a single-mode assumption and $U_{cr}=0.1965$ L/s using the three-mode approximation. Such results indicate that a single-mode reduced-order model is sufficient to predict the local dynamics of the response around the static equilibria.

To see how these trends are reflected in the non-linear system's response, Equations (41), (42), and (43) were integrated numerically using a single- and three-mode expansions. The resulting bifurcation diagram shown in Figure 7, which depicts variation of the steady-state output voltage with the flow rate, clearly demonstrates negligible differences between the single- and three-mode response. This again demonstrates the accuracy of the single-mode approximation. As such, further analysis presented in this manuscript will be based on a reduced-order model consisting of a single mode.

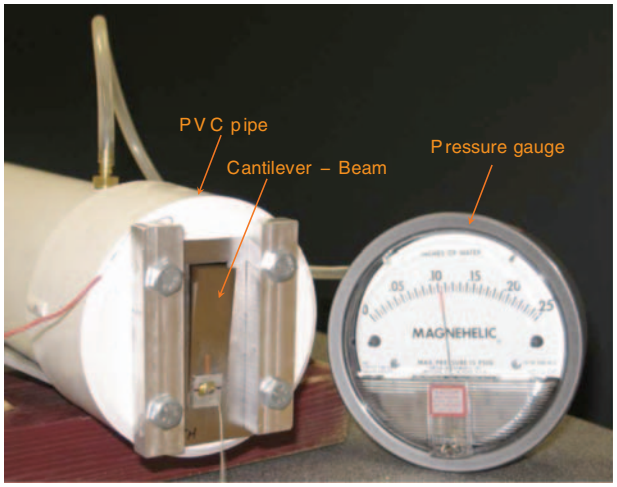


***Figure 8.*** *Wind-driven autonomous beam vibrations.*

## EXPERIMENTAL VALIDATIONS

Figure 8 depicts the experimental configuration employed to investigate the validity of the proposed model. A 2.4 L air chamber is constructed using a PVC pipe with inside diameter of 76.2 mm, closed with two

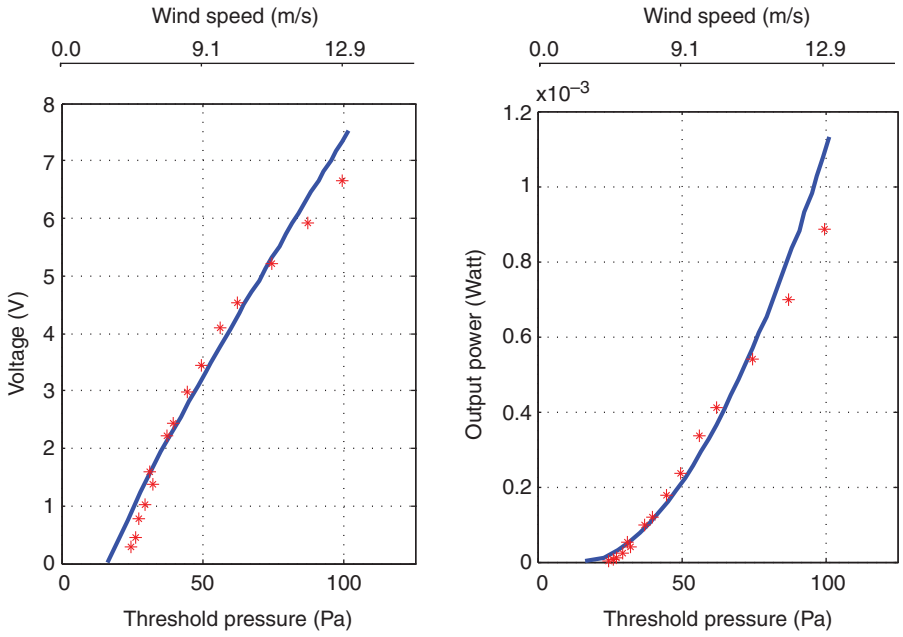


***Figure 9.*** *Variation of the voltage and output power with the wind speed. Asterisks represent experimental data.*

PVC caps. On one end cap, the cantilever beam is mounted over the aperture/slot as shown in the figure. To accommodate the beam, the aperture is made slightly larger than the beam. From the other end of the chamber, air is supplied using an air pump through a small hole at the center of the cap. To validate the model, a beam is cut from a 0.3-mm thick aluminum sheet which has the geometric and material properties listed in Table 1.

In the experiments, the air pressure is increased incrementally from 0 to 100 Pa. At each step, the mean pressure at the beam surface is measured using a pressure gage and the corresponding output voltage at different pressures is recorded. The air pressure is then slowly decreased from 100 Pa until the beam vibration ceases. Once again, the output voltage at different pressures is recorded. It was observed that there are not much differences between the voltage values measured at both directions of the pressure sweep. As such, only the average value is reported. The natural frequency of the limit cycle was observed to have slight variation with the inflow rate and was recorded at about 85 Hz. Figure 9 shows variation of the voltage and output power of the device with the wind speed over an electric load of 50 kΩ. The experimental results are also compared to numerical simulations obtained via long-time integration of Equations (41), (42), and (43).

As shown in Figure 9, there is fairly good agreement between the theoretical and experimental findings and the Hopf bifurcation point is well estimated. The beam is activated at a moderate cut-on wind speed of approximately 6.95 m/s. The experiments further reveal that the transition from the static position to the limit-cycle oscillations is continuous without sudden jumps. This indicates that the bifurcation is *supercritical* for the chosen design parameters which agrees with the predictions of the mathematical model. The 0.1−0.8 mW of output power attained at wind speeds ranging between 7.5 and 12.5 m/s clearly demonstrate the potential for using such concept to power and operate many microcontroller chips, health-monitoring sensors, and wireless transponders (Bracke et al., 2007; Kim et al., 2007). However, such results by no means represent the optimal performance of this device.

## BIFURCATION'S NORMAL FORM

As shown previously in Figure 2(a), when the bifurcation is *supercritical* and the flow rate exceeds the threshold value, small-amplitude limit-cycle oscillations about the former static position are born. On the other hand, when the bifurcation is *subcritical* as shown in Figure 2(b), the output voltage jumps to a distant attractor which can be another fixed point, a large-amplitude limit cycle, or even a chaotic attractor. In most engineering applications, subcritical bifurcations are considered dangerous because they can cause structural failure. In our study, however, a subcritical Hopf bifurcation means large amplitude oscillations at lower wind speeds which could imply an enhanced performance of the harvester.

In this section, we utilize the method of multiple scales (Nayfeh, 1981) to study the normal form and nature of the bifurcation responsible for the onset of limit-cycle oscillations of the MPG. To implement the method of

multiple scales, we first non-dimensionalize the coupled ordinary differential equations governing the response. Toward that end, we introduce the following dimensionless quantities:

$$\bar{q} = \frac{q}{L}, \quad \bar{t} = t\omega_n, \quad \bar{V} = \frac{C_p}{\theta} V, \quad \bar{P}_A = \frac{P_A}{P_\infty}, \quad \bar{U} = \frac{U_0}{U_{cr}}, \quad (46)$$

where $P_\infty$ is the ambient pressure and $U_{cr}$ is the critical inflow rate. Introducing Equation (46) into Equations (41), (42), and (43) yields:

$$\ddot{\bar{q}} + 2\zeta\dot{\bar{q}} + \bar{q} + \Gamma\bar{q}^3 + \Lambda\left[\bar{q}^2\ddot{\bar{q}} + \bar{q}\dot{\bar{q}}^2\right] + \theta_1\bar{V} + \theta_2\bar{q}^2\bar{V} = \Delta\bar{P}_A, \quad (47)$$

$$\dot{\bar{V}} = -\alpha\bar{V} + \theta_3\dot{\bar{q}} + \theta_4\bar{q}^2\dot{\bar{q}}, \quad (48)$$

$$\dot{\bar{P}}_A = \beta_1\left[\bar{U}U_{cr} - C_c\bar{A}(\bar{q})\left(\frac{2P_\infty}{\rho}\bar{P}_A\right)^{\frac{1}{2}} - \Pi\dot{\bar{q}}\right], \quad (49)$$

where

$$\Gamma = \frac{\mathcal{A}L^2}{\omega_n^2}, \quad \Lambda = \mathcal{B}L^2, \quad \theta_1 = \frac{\mathcal{D}\theta}{L\omega_n^2 C_p}, \quad \theta_2 = \frac{\mathcal{C}L\theta}{C_p\omega_n^2}, \quad \Delta = \frac{\mathcal{E}P_\infty}{L\omega_n^2}, \quad \alpha = \frac{1}{RC_p\omega_n}, \quad \theta_3 = \frac{\mathcal{F}C_pL}{\theta}, \quad \theta_4 = \frac{\mathcal{G}L^3C_p}{\theta}, \quad \beta_1 = \frac{\rho c^2}{V_r\omega_n P_\infty}, \quad \Pi = \mathcal{E}L\omega_n, \quad (50)$$

$$\bar{A}(\bar{q}) = 2L\int_0^L \left[\phi^2(s)L^2\bar{q}^2 + b^2\right]^{\frac{1}{2}}\mathrm{d}s + W_b\left[\phi^2(L)L^2\bar{q}^2 + b^2\right]^{\frac{1}{2}} \quad (51)$$

To facilitate the implementation of the method of multiple scales, the integral of Equation (51) is approximated using our knowledge of the form of $\phi(s)$. This permits writing the total exit area of the aperture in terms of the tip deflection as (Fletcher, 1992):

$$\bar{A}(\bar{q}) = 2L\left[0.16\phi^2(L)\bar{q}^2L^2 + b^2\right]^{\frac{1}{2}} + W_b\left[\phi^2(L)\bar{q}^2L^2 + b^2\right]^{\frac{1}{2}} \quad (52)$$

Figure 10 shows a comparison between the exact and the approximated values of the aperture area. Two sets of curves are generated by evaluating Equations (51) and (52) for a given range of tip deflections. The first set is obtained for a small gap width, $b = 0.1$ mm, while the second set is calculated for a relatively large gap width, $b = 0.5$ mm. It can be seen that in both cases, the approximated aperture area is well-estimated using Equation (52), and that the error in the estimation increases by increasing the gap width.

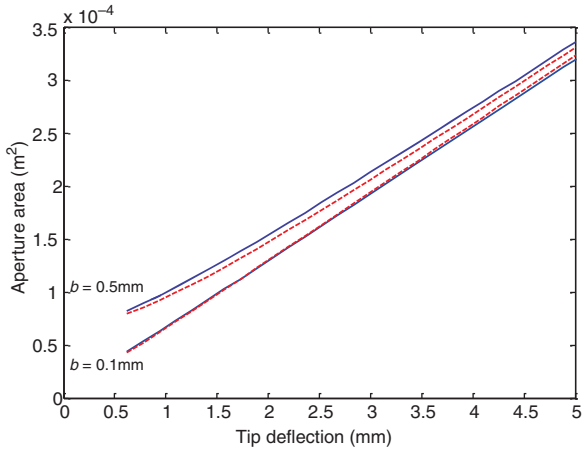


***Figure 10.*** *Aperture area comparison for different gap widths: Exact (Solid), Approximated (dashed).*

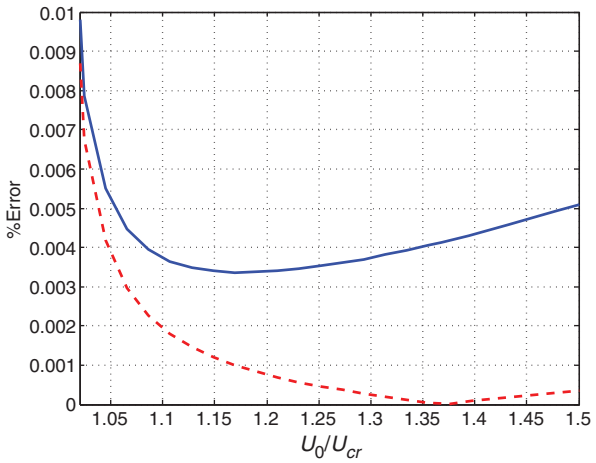


***Figure 11.*** *Steady-state error resulting from neglecting the non-linearity as function of $\bar{U}$: $\bar{q}$ (solid), $\bar{V}$ (dashed).*

To allow for correct scaling of the non-linear terms associated with the non-linear strain–displacement relationship in Equation (8); we asses their influence on the non-linear system's response. As such, we integrate Equations (47) and (48) numerically and obtain the steady-state non-dimensional voltage, $\bar{V}$, and deflection $\bar{q}$ with and without including the non-linear terms. Figure 11 demonstrates that the error resulting from neglecting the non-linear terms remains within 0.01% for both $\bar{q}$ and $\bar{V}$. This implies that these cubic non-linearity terms have a negligible influence on the system's response and therefore can be neglected.

**Implementation of the Method of Multiple Scale**

We express the system response as the sum of static and dynamic components as follows:

$$\begin{aligned}\bar{q} &= q_s + q_d,\\ \bar{P}_A &= P_s + p_d,\\ \bar{V} &= V_s + V_d,\end{aligned} \tag{53}$$

where the subscript $s$ denotes the static part and $d$ denotes the dynamic component. The quantities $q_s$, $P_s$, and $V_s$ represent, respectively, the static deflection, pressure, and output voltage for a given input flow rate $U_0$. These can be obtained by setting the time derivatives in Equations (47)–(49) to zero and solving the resulting algebraic equations. Substituting Equation (53) back into Equations (47), (48), and (49), expanding the aperture area, $\bar{A}(\bar{q})$, in a Taylor series up to cubic terms, and separating the dynamic and static terms, yield the following set of equations:

$$\ddot{q}_d + 2\zeta\dot{q}_d + q_d + \theta_1 V_d = \Delta p_d, \tag{54a}$$

$$\dot{V}_d = -\alpha V_d + \theta_3\dot{q}_d, \tag{54b}$$

$$\begin{aligned}\dot{p}_d = -\Big(&C_1 p_d + C_2 q_d + C_3 p_d q_d + C_4 p_d^2 + C_5 q_d^2 + C_6 q_d^3\\ &+ C_7 p_d^2 q_d + C_8 p_d q_d^2 + C_9 p_d^3 + C_{10}\dot{q}_d\Big),\end{aligned} \tag{54c}$$

where

$$\begin{aligned}&C_1 = \frac{\beta_1\beta_2\alpha_0}{2P_s}, \quad C_2 = \beta_1\beta_2\alpha_1, \quad C_3 = \frac{\beta_1\beta_2\alpha_1}{2P_s},\\ &C_4 = -\frac{\beta_1\beta_2\alpha_0}{8P_s^2}, \quad C_5 = \beta_1\beta_2\alpha_2, \quad C_6 = \beta_1\beta_2\alpha_3,\\ &C_7 = -\frac{\beta_1\beta_2\alpha_1}{8P_s^2}, \quad C_8 = \frac{\beta_1\beta_2\alpha_2}{2P_s}, \quad C_9 = \frac{\beta_1\beta_2\alpha_0}{16P_s^3},\\ &C_{10} = \beta_1\Pi, \quad \beta_2 = C_c\sqrt{\frac{2P_\infty}{\rho}},\\ &\alpha_n = \sqrt{P_s}\frac{d^n\bar{A}(\bar{q})}{d\bar{q}^n}\Big|_{q_s}, \quad n = 0.3\end{aligned} \tag{55}$$

The time dependence is also expanded into multiple time scales as:

$$\begin{aligned}&T_n = \epsilon^n t, \quad n = 0, 1, 2,\\ &\frac{d}{dt} = D_0 + \epsilon D_1 + \epsilon^2 D_2 + O(\epsilon^3),\\ &\frac{d^2}{dt^2} = D_0^2 + 2\epsilon D_0 D_1 + \epsilon^2 D_1^2 + 2\epsilon^2 D_0 D_2 + O(\epsilon^3),\end{aligned} \tag{56}$$

where $\epsilon$ is a bookkeeping parameter that will be set to unity at the end of the analysis and $D_n = \partial/\partial T_n$. We seek a solution in the form:

$$\begin{aligned}q_d(t;\epsilon) &= q_0(T_0, T_1, T_2) + \epsilon q_1(T_0, T_1, T_2)\\ &\quad + \epsilon^2 q_2(T_0, T_1, T_2) + \ldots\\ V_d(t;\epsilon) &= V_0(T_0, T_1, T_2) + \epsilon V_1(T_0, T_1, T_2)\\ &\quad + \epsilon^2 V_2(T_0, T_1, T_2) + \ldots\\ p_d(t;\epsilon) &= p_0(T_0, T_1, T_2) + \epsilon p_1(T_0, T_1, T_2)\\ &\quad + \epsilon^2 p_2(T_0, T_1, T_2) + \ldots\end{aligned} \tag{57}$$

We scale the terms with quadratic and cubic nonlinearity in Equation (54c), and scale the damping, $\zeta$, the voltage, $V_d$, and the pressure, $p_d$ in Equation (54a) to appear at the second order of the perturbation problem. i.e., $C_i = \epsilon C_i$, where $i = 3.9$, $\zeta = \epsilon\zeta$, $\Delta = \epsilon\Delta$, and $\theta_1 = \epsilon\theta_1$. Now, substituting Equations (56) and (57) into Equation (54), and equating coefficients of like power of $\epsilon$ yields:

($\epsilon^0$):

$$D_0^2 q_0 + q_0 = 0, \tag{58a}$$

$$D_0 V_0 - \alpha V_0 = \theta_3 D_0 q_0, \tag{58b}$$

$$D_0 p_0 + C_1 p_0 = -(C_2 q_0 + C_{10} D_0 q_0), \tag{58c}$$

($\epsilon^1$):

$$D_0^2 q_1 + q_1 = \Delta p_0 - 2D_1 D_0 q_0 - 2\zeta D_0 q_0 - \theta_1 V_0, \tag{59a}$$

$$D_0 V_1 - \alpha V_1 = \theta_3(D_0 q_1 + D_1 q_0) - D_1 V_0, \tag{59b}$$

$$\begin{aligned}D_0 p_1 + C_1 p_1 = -(&D_1 p_0 + C_2 q_1 + C_3 p_0 q_0 + C_4 p_0^2 + C_5 q_0^2\\ &+ C_6 p_0 q_0^2 + C_7 p_0^2 q_0 + C_8 p_0^3 + C_9 q_0^3\\ &+ C_{10} D_0 q_1 + C_{10} D_1 q_0),\end{aligned} \tag{59c}$$

($\epsilon^2$):

$$\begin{aligned}D_0^2 q_2 + q_2 =&\Delta p_1 - \theta_1 V_1 - 2\zeta(D_0 q_1 + D_1 q_0)\\ &- (D_1^2 + 2D_2 D_0) q_0 - 2D_1 D_0 q_1,\end{aligned} \tag{60a}$$

$$\begin{aligned}D_0 V_2 - \alpha V_2 = &\theta_3(D_0 q_2 + D_1 q_1 + D_2 q_0)\\ &- D_1 V_1 - D_2 V_0,\end{aligned} \tag{60b}$$

$$\begin{aligned}D_0 p_2 + C_1 p_2 = -[&D_1 p_1 + D_2 p_0 + C_2 q_2 + C_3(p_0 q_1 + p_1 q_0)\\ &+ 2C_4 p_0 p_1 + 2C_5 q_0 q_1\\ &+ C_6(2p_0 q_0 q_1 + p_1 q_0^2)\\ &+ C_7(p_0^2 q_1 + 2p_0 p_1 q_0)\\ &+ 3C_8 p_0^2 p_1 + 3C_9 q_0^2 q_1\\ &+ C_{10}(D_0 q_2 + D_1 q_1 + D_2 q_0)],\end{aligned} \tag{60c}$$

The solution of the first-order problem, Equation (58a), can be expressed as:

$$q_0 = A(T_1, T_2)e^{iT_0} + cc, \tag{61}$$

where $A$ is a complex-valued function that will be determined at a later stage in the analysis and $cc$ is the complex conjugate of the preceding term. Substituting Equation (61) into Equations (58b) and (58c), and solving for the corresponding variable, one obtains:

$$V_0 = XAe^{iT_0} + cc, \tag{62}$$

$$p_0 = \frac{C_2 + iC_{10}}{C_1 + i}Ae^{iT_0} + cc, \tag{63}$$

where

$$X = \frac{i\theta_3}{i - \alpha}.$$

Substituting Equations (61), (62), and (63) into Equation (59a) yields:

$$D_0^2 q_1 + q_1 = -\left(2iD_1A + 2i\zeta A - \Delta\frac{C_2 + iC_{10}}{C_1 + i}A + \theta_1 XA\right)e^{iT_0} + cc. \tag{64}$$

Next, we eliminate any secular terms (terms having the factor $\pm e^{iT_0}$), and obtain:

$$D_1A = \frac{1}{2}i\left[2i\zeta A - \Delta\frac{C_2 + iC_{10}}{C_1 + i}A + \theta_1 XA\right]. \tag{65}$$

Considering Equation (65), the solution of the second-order problem, Equation (59a), is $q_1 = 0$. Substituting $q_0$, $V_0$, $p_0$, and $q_1$ into Equations (59b) and (59c) and solving for $V_1$ and $p_1$, respectively, yields:

$$V_1 = -\frac{\theta_3\alpha}{(i - \alpha)^2}D_1Ae^{iT_0} + cc, \tag{66}$$

$$p_1 = -\frac{1}{C_1}\left[C_3X + C_4X\bar{X} + C_5\right]A\bar{A} - \frac{Y_1A^2\bar{A}}{C_1 + i}e^{iT0} - \frac{Y_2A^2}{C_1 + 2i}e^{2iT0} - \frac{Y_3A^3}{C_1 + 3i}e^{3iT0}\frac{(X + C_{10})D_1A}{C_1 + i}e^{iT_0}, \tag{67}$$

where

$$Y_1 = 2C_6X + C_6\bar{X} + 2C_7X\bar{X} + C_7X^2 + 3C_8X^2\bar{X} + 3C_9,$$
$$Y_2 = C_3X + C_4X^2 + C_5,$$
$$Y_3 = C_6X + C_7X^2 + C_8X^3 + C_9,$$

and $\bar{A}$ and $\bar{X}$ are the complex conjugate of $A$ and $X$, respectively. Substituting $q_0$, $q_1$, $V_1$, and $p_1$ into Equation (60a) and eliminating the terms that lead to secular terms yields:

$$D_2A = \mathbf{F_1}\bar{A}A^2 + \mathbf{F_2}A, \tag{68}$$

where $\mathbf{F}_1$ and $\mathbf{F}_2$ are functions of $\zeta$, $\alpha$, $\Delta$, $\theta_1$, $\theta_3$, $U_0$, and $C_n$. Using the method of reconstitution (Nayfeh, 2005), one can write:

$$\frac{dA}{\mathrm{d}t}(t;\epsilon) = \epsilon D_1A + \epsilon^2 D_2A + \ldots. \tag{69}$$

Substituting Equations (65) and (68) into Equation (69), expressing $A$ in the polar form $A = \frac{1}{2}ae^{i\beta}$, where $a$ and $\beta$ are real-valued amplitude and phase, separating real and imaginary parts, and setting $\epsilon = 1$, we obtain:

$$\dot{a} = \mu_1a^3 + \mu_2a \tag{70}$$

$$\dot{\beta} = \gamma_1a^2 + \gamma_2 \tag{71}$$

where $\mu_1$, $\mu_2$, $\gamma_1$, and $\gamma_2$ are functions of the design parameters and the inflow rate. Equations (70) and (71) represent the normal form for a Hopf bifurcation with $\mu_2$ equal to zero at the critical inflow rate, $U_{cr}$. To solve for the steady-state amplitude of the response, we set $\dot{a} = 0$ in Equation (70) and obtain:

$$a_0 = 0, \quad a_0 = \pm\sqrt{-\frac{\mu_2}{\mu_1}}, \quad \text{when} \quad \frac{\mu_2}{\mu_1} < 0 \quad \text{and} \quad a_0 = 0, \quad \text{when} \quad \frac{\mu_2}{\mu_1} > 0. \tag{72}$$

Substituting the non-zero fixed point back into Equation (61), we obtain the following approximate analytical solution for the steady-state limit-cycle oscillations of Equations (54) as:

$$q_d = a_0\cos(\omega_m t + \beta_0) + O(a^3), \tag{73}$$

$$V_d = a_0\mathcal{F}\cos(\omega_m t + \beta_0) + O(a_0^3), \tag{74}$$

where $\beta_0$ and $\mathcal{F}$ are constants, and

$$\omega_m = (1 + \dot{\beta}) + O(a_0^3) = 1 + \gamma_1a_0^2 + \gamma_2 + O(a_0^3) \tag{75}$$

is the analytical approximation of the limit cycle's frequency. It is important to bear in mind that the solutions acquired via the method of multiple scales are accurate for small range of the inflow rate beyond its critical value. Hence, the accuracy is expected to deteriorate as $U_0$ becomes much larger than the critical value.

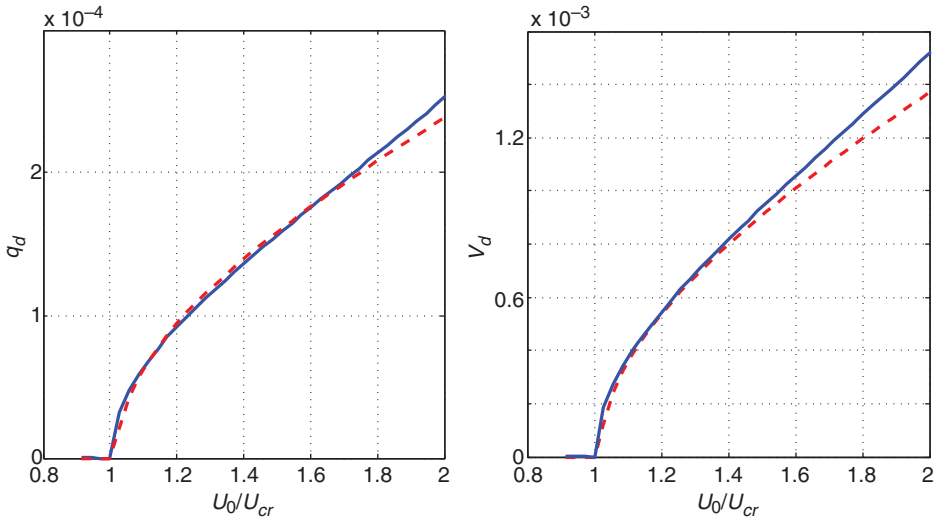


***Figure 12.*** *Bifurcation diagrams constructed by the method of multiple scales (dashed) and numerically (solid): left for $q_d$ and right for $V_d$.*

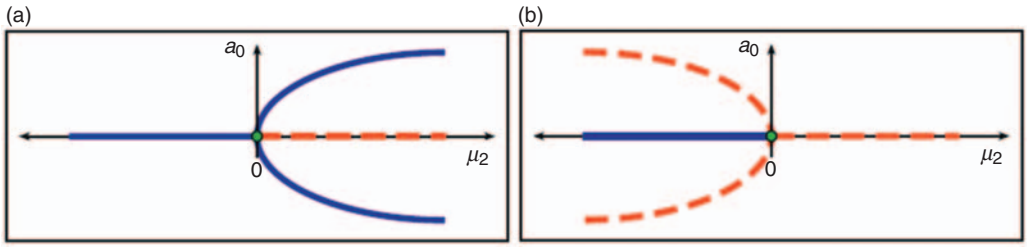


***Figure 13.*** *Sketches of fixed points and their stability: (a) supercritical Hopf bifurcation $\mu_1 < 0$ and (b) subcritical Hopf bifurcation $\mu_1 > 0$.*

In Figure 12, we compare the analytical approximation (dashed lines) with the numerical solutions (solid lines) of Equations (54) for different values of $U_0$. The figure demonstrates good agreement between the analytical and numerical solutions for moderate values of $U_0/U_{cr}$. As the ratio between $U_0$ and $U_{cr}$ increases beyond 1.5 the analytical solution starts to deviate from the numerical integration.

To determine the nature of the Hopf bifurcation, the stability of the steady-state solutions is determined by evaluating the Jacobian of the modulation equations, Equations (70) and (71) at the fixed points. This yields:

$$J(a_0) \equiv \frac{\mathrm{d}\dot{a}}{\mathrm{d}a}\bigg|^{a_0} = \begin{cases} \mu_2, & a_0 = 0 \\ -2\mu_2, & a_0 = \pm\sqrt{-\frac{\mu_2}{\mu_1}} \end{cases} \tag{76}$$

By inspecting Equation (76), it becomes evident that, when $\mu_1\ \mu_2 > 0$, only the trivial solution exists and it is stable for $\mu_2 < 0$ and unstable for $\mu_2 > 0$. On the other hand , when $\mu_1\ \mu_2 < 0$, three fixed points exist; when $\mu_2 > 0$ the trivial fixed point is unstable while the non-trivial fixed points are stable resulting in a supercritical Hopf bifurcation as illustrated in Figure 13(a). On the other hand, when $\mu_2 < 0$, the zero fixed point is stable while the non trivial fixed points are unstable yielding a subcritical Hopf bifurcation as illustrated in Figure 13(b).

By virtue of the previous discussion, it becomes evident that the signs of $\mu_1$ and $\mu_2$ determine the nature of the bifurcation at the linear stability boundary. Figure 14(a) and (c) depict, respectively, variations of $\mu_1$ and $\mu_2$ for a range of the chamber volume, $V_r$, and beam length, $L_b$. The other design parameters and material properties of the beam and the piezoelectric layer are kept constant as listed in Table 1. Results indicate that $\mu_1$ is always negative while $\mu_2$ remains positive throughout the range considered in the figure. This implies that a supercritical Hopf bifurcation always occurs for the values of $L_b$ and $V_r$ considered.

It is worth mentioning that the values of $\mu_1$ and $\mu_2$ exist only when $U_{cr}$ exists. Otherwise, no Hopf bifurcation occurs in the first place. Figure 14(b) and (d) represent two-dimensional projection of Figure 14(a) and (c), respectively. The shaded regions depict the combinations of ($L_b$, $V_r$) which yield a real value for $U_{cr}$, whereas the unshaded regions represent combinations of ($L_b$, $V_r$) for which no bifurcation occurs. In those regions, the beam does not oscillate regardless of how large the inflow rate is.

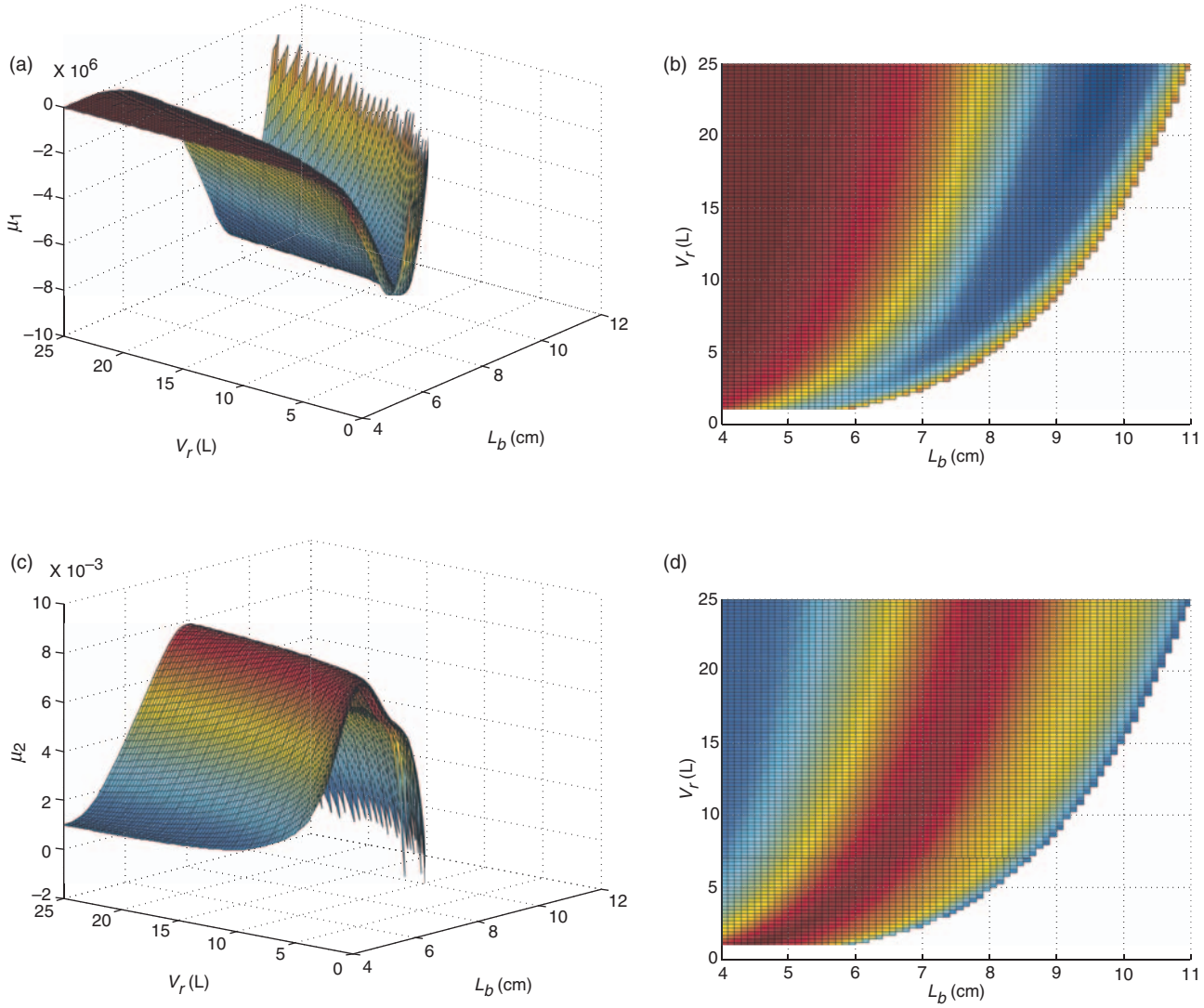


***Figure 14.*** *Variation of $\mu_1$ and $\mu_2$ for different design parameters: (a) $\mu_1$, (b) top view of $\mu_1$, (c) $\mu_2$, and (d) top view of $\mu_2$.*

## CONCLUSION

In this effort, we developed a non-linear reduced-order electro-mechanical model to capture the response behavior of a self-excited MPG. The generator consists of a piezoelectric uni-morph beam embedded within a cavity to mimic vibrations of harmonica's reeds when subjected to air flow. To obtain the equations of motion, we treated the problem at two levels. At the first level, we used Hamilton's principle combined with the non-linear Euler–Bernoulli beam theory, the inextensibility condition, and the linear constitutive equations of piezoelectricity to obtain the non-linear partial differential equation governing the transversal dynamics of the beam and the ordinary differential equation governing the output voltage of the harvester. At the second level, we used the steady Bernoulli's equation in conjunction with the continuity equation to determine the relation between the exciting pressure at the surface of the beam, the input flow rate of air, and the beam deflection. The resulting system of equations was then discretized using a Galerkin expansion into a set of non-linearly coupled ordinary differential equations. A convergence analysis was carried out to determine the minimum number of modes to be kept in the reduced-order model. It was determined that a reduced-order model consisting of a single mode is accurate enough to predict the static and dynamic behavior of the harvester for a large range of inflow rate. The resulting reduced-order model was validated against experimental data showing excellent agreement. Finally, using the method of multiple scales, we developed an approximate analytical solution of the resulting reduced-order model near the linear stability boundary and studied the normal form of the resulting bifurcation. We observed that a Hopf bifurcation of the supercritical nature is responsible for the onset of

limit-cycle oscillations. The bifurcation remains supercritical as two of the design parameters, namely, the beam's length and chamber's volume are varied. The model obtained in this study provides the platform for future optimization studies aiming to minimize the cut-on wind speed and maximize the output power of the generator.

## ACKNOWLEDGMENT

The authors acknowledge the financial support of the National Science Foundation (NSF) under Grant No. CMMI-1000667.

## REFERENCES

Allen, J.J. and Smits, A.J. 2001. "Energy Harvesting Eel," *Fluids and Structures*, 15:629–640.

Arms, S.W., Townsend, C.P., Churchill, D.L., Galbreath, G.H. and Mundell, S.W. 2005. "Power Management for Energy Harvesting Wireless Sensors," In: *Proceedings of the Smart Structures and Materials Conference, SPIE*, San Diego, CA, p. 5763, 267–275.

Baerta, K., Gyselinckxa, B., Torfsa, T., Leonova, V., Yazicioglua, F., Brebelsa, S., Donnaya, S., Vanfleterena, J., Beyna, E. and Van Hoof, C. 2006. "Technologies for Highly Miniaturized Autonomous Sensor Newtorks," *Microelectronics Journal*, 37:1563–1568.

Barrero-Gil, A., Alonso, G. and Sanz-Andres, A. 2010. "Energy Harvesting from Transverse Galloping," *Sound and Vibration*, 329:2873–2883.

Bracke, W., Merken, P., Puers, R. and Van Hoof, C. 2007. "Generic Architectures and Design Methods for Autonomous Sensors," *Sensors and Actuators A*, 135:881–888.

duPlessis, A.J., Huigsloot, M.J. and Discenzo, F.D. 2005. "Resonant Packaged Piezoelectric Power Harvester for Machinery Health Monitoring," In: *Proceedings of Smart Structures and Materials Conference, SPIE*, San Diego, CA, p. 5762.

duToit, N. and Wardle, B. 2007. "Experimental Verification of Models for Microfabricated Piezoelectric Energy Harvesters," *AIAA Journal*, 45:1126–1137.

Erturk, A. and Inman, D. 2008. "A Distributed Parameter Electromechanical Model for Cantilevered Piezoelectric Energy Harvesters," *Journal of Vibration and Acoustics, Transaction of ASME*, 130:1–14.

Erturk, A., Vieira, W.G.R., De Marqui, C. and Inman, D.J. 2010. "On the Energy Harvesting Potential of Piezoaeroelastic Systems," *Applied Physics Letters*, 96:184102.

Fletcher, N.H. 1992. "Autonomous Vibration of Simple Pressuer-Controlled Valves in Gas Flows," *Journal of Acoustic Society of America*, 93:2172–2180.

Gregori, S., Li, Y., Li, H., Liu, J. and Maloberti, F. 2004. "2.45 GHz Power and Data Transmission for a Low-Power Autonomous Sensors Platform," *ISLPED 04*, pp. 269–273.

Inman, D.J. and Grisso, B.L. 2006. "Towards Autonomous Sensing," In: *Proceedings of Smart Structures and Materials Conference, SPIE*, San Diego, CA, p. 61740T.

Kim, J.W., Takao, H., Sawada, K. and Ishida, M. 2007. "Integrated Inductors for RF Transmitters in CMOS/MEMS Smart Microsensor Systems," *Sensors*, 7:1387–1398.

Liao, J.C., Beal, D., Lauder, J. and Triantafyllou, M.S. 2003. "Fish Exploiting Vortices Decrease Muscle Activity," *Science* 302:1566–1569.

Lissaman, P. 1983. "Low-Reynolds-Number Airfoils," *Annual Review in Fluid Mechanics*, 15:223–239.

Meirovitch, L. 1997. *Principles and Technqiues in Vibrations*, Prentice Hall, New Jersey, NJ.

Mitcheson, P., Yeatman, E., Rao, K., Holmes, S. and Green, T. 2008. "Energy Harvesting from Human and Machine Motion for Wireless Electronic Devices," *Proceedings of the IEEE*, 96:1457–1486.

Munson, B., Young, R., Okiishi, D. and Huebsch, T. 2009. *Fundamentals of Fluid Mechanics*, John Wiley and Sons, Inc, NY.

Nayfeh, A.H. 1981. *Introduction to Perturbation Techniques*, Wiley-Interscience, New York.

Nayfeh, A.H. 2004. *Linear and Nonlinear Structural Mechanics*, Wiley, New Jersey, NJ.

Nayfeh, A.H. 2005. "Resolving Controversies in the Application of the Method of Multiple Scales and The Generalized Method of Averaging," *Nonlinear Dynamics*, 40:61–102.

Osorio, T. and Daqaq, M.F. 2009. "On the Reduced-Order Modeling of Energy Harvesters," *Journal of Intelligent Materials Systems and Structures* Published Online, 20(16):2003–2016.

Paradiso, J.A. and Starner, T. 2005. "Energy Scavenging for Mobile and Wireless Electronics," *IEEE Pervasive Computing*, 4:18–27.

Ricot, D., Causse, R. and Misdarris, N. 2005. "Aerodynamic Excitation and Sound Production of Blow-Closed Free Reeds without Acoustic Coupling: The Example of the Accordion Reed," *Journal of Acoustic Society of America*, 117:2279–2290.

Robbins, W.P., Marusic, I., Morris, D. and Novak, T.O. 2006. "Experiments in Direct Energy Extraction through Flapping Foils," In: *Proceedings of 2006 ASME International Mechanical Engineering Congress and Exposition*, Chicago, IL.

Roundy, S. and Wright, P.K. 2005. "A Piezoelectric Vibration-Based Generator for Wireless Electronics," *Journal of Intelligent Materials and Structures*, 16:809–823.

Roundy, S., Wright, P.K. and Rabaey, J. 2003. "A Study of Low Level Vibrations as a Power Source for Wireless Sensor Nodes," *Computer Communications*, 26:1131–1144.

Simpson, B.J., Hover, F.S. and Triantafyllou, M.S. 2008. "Experiments in Direct Energy Extraction Through Flapping Foils," In: *Proceedings of the Eighteenth International Offshore and Polar Engineering Conference*, Vancouver, Canada, pp. 370–376.

St. Clair, D., Bibo, A., Sennakesavababu, V.R., Daqaq, M.F. and Li, G. 2010. "A Scalable Concept for Micropower Generation Using Flow-Induced Self-Excited Oscillations," *Applied Physics Letters*, 96:144103.

St. Clair, D., Stabler, C., Daqaq, M.F., Luo, J. and Li, G. 2009. "A Smart Device for Harnessing Energy from Aerodynamic Flow Fields," In: *Proceedings of the ASME International Mechanical Engineering Congress and Exposition, IMECE 2009*, Lake Buena Vista, Fl.

St. Hilaire, A.O. 1976. "Analytical Prediction of The Non-Linear Response of A Self-Excited Structure," *Journal of Sound and Vibrations*, 27:185–205.

Strogatz, S.H. 2000. *Nonlinear Dynamics and Chaos: With Applications to Physics, Biology, Chemistry and Engineering*, Westview, Cambridge, MA.

Tang, L., Padoussis, P. and Jang, J. 2009. "Cantilevered Flexible Plates in Axial Flow: Energy Transfer and the Concept of Flutter-mill," *Sound and Vibration*, 326:263–276.

Tarnopolsky, A.Z., Fletcher, N.H. and Lai, J.C.S. 2000. "Oscillating Reed Valves-An Experimental Study," *Journal of the Acoustic Society of America*, 108:400–406.

Tarnopolsky, A.Z., Lai, J. and Fletcher, N. 2001. "Flow Structures Generated by Pressure-Controlled Self-Oscillating Reed Valves," *Journal of Sound and Vibrations*, 247:213–226.

Zhu, Q., Haase, M. and Wu, C.H. 2009. "Modelling the Capacity of a Novel Flow-energy Harvester," *Applied Mathematical Modelling*, 33:2207–2217.